Materials Advances

PAPER

View Article Online
View Journal | View Issue

Cite this: *Mater. Adv.*, 2025, **6**, 6724

Effect of calcination temperature on nano-cobalt ferrite synthesized by a sol–gel method for modification of its structural, morphological, magnetic, electrical and optical properties

Md. Farid Ahmed, *[a] Afia Yasmin,[ac] Bristy Biswas,[a] Md. Lutfor Rahman,[a] Juliya Khanam,[a] Rabeya Jahan Rakhi,[c] Mahmuda Hakim,[b] Md. Sahadat Hossain,[a] Firoz Ahmed,[d] Israt Jahan Lithi[e] and Nahid Sharmin[a]

Synthesis of cobalt ferrite ($CoFe_2O_4$) nanoparticles (NPs) through a sol–gel process is an efficient and cost-effective approach. This process is carried out at different calcination temperatures (500 °C, 600 °C, 700 °C, 800 °C, 900 °C and 1000 °C) using cobalt nitrate [$Co(NO_3)_2 \cdot 6H_2O$], ferric nitrate [$Fe(NO_3)_3 \cdot 9H_2O$], citric acid ($C_6H_8O_7 \cdot H_2O$), glycerol ($C_3H_8O_3$), and ammonium hydroxide (NH_4OH). It is found that different calcination temperatures affect the size of the crystallite produced, *i.e.*, at higher temperature the size of the crystals increases. To study the structural, optical, magnetic and dielectric properties of the cobalt ferrite nanoparticles synthesized by a sol–gel method, characterization techniques such as X-ray diffraction (XRD), simultaneous thermal analysis (STA), vibrating sample magnetometry (VSM), scanning electron microscopy (SEM) and Fourier transform infrared (FTIR) spectroscopy were carried out. XRD proved the face centered cubic structure of the NPs. At 1000 °C the sample T6 exhibited a higher zeta potential proving the stability of the solution. The crystallite size and lattice strain were measured by the Debye–Scherrer (D–S) method, Williamson–Hall (W–H) process, Halder–Wagner (H–W) method and size–strain plot (SSP) technique. XRD data confirm the presence of the single spinel phase of cobalt ferrite NPs for all the samples. The sample T1 showed the lowest crystallite size, and the crystallite size ranged from 33 nm to 169 nm for the T6 sample. Two FTIR absorption bands observed at about 402–403 cm^{-1} and 576–580 cm^{-1} are due to the octahedral M–O bond and the M–O bond at the tetrahedral site in the spinel cobalt ferrite, respectively. The SEM micrographs showed that the produced NPs are spherical in shape and homogenously distributed. The average particle size is found to be 46.72 nm for the sample annealed at 800 °C. The maximum saturation magnetization was found to be around 85–62 emu g^{-1}. The band gap energy was found using the Kubelka–Munk method, and it was found that as the annealing temperature increases the size of crystals increases and band gap energy ranges from 3.00 to 3.52 eV, respectively. Thus the sol–gel method can be used to modify the crystallite size at different calcination temperatures.

Received 8th March 2025,
Accepted 9th August 2025

DOI: 10.1039/d5ma00209e

rsc.li/materials-advances

1. Introduction

Nanotechnology has revolutionized materials science through the development of materials with specific properties that can be very different from their bulk counterparts. Among the various nanomaterials, magnetic nanoparticles have gained immense attention due to their fine magnetic, optical, dielectric, structural and electrical properties. Cobalt ferrite ($CoFe_2O_4$) nanoparticles are among such highly studied magnetic nanoparticles. They are used in a variety of different fields including medical diagnosis, catalytic degradation, MRI, sensors, drug delivery, waste-water treatment systems, solar cells, power transformers, magnetic hyperthermia microwave

---

[a] Institute of Glass and Ceramic Research and Testing (IGCRT), Bangladesh Council of Scientific and Industrial Research (BCSIR), Dhaka-1205, Bangladesh. E-mail: ahmedfarid@bcsir.gov.bd
[b] Biomedical and Toxicological Research Institute, Bangladesh Council of Scientific and Industrial Research (BCSIR), Dhaka-1205, Bangladesh
[c] Department of Chemistry, Begum Badrunnesa Govt. Girls College, Dhaka-1211, Bangladesh
[d] BCSIR Rajshahi Laboratories, Bangladesh Council of Scientific and Industrial Research (BCSIR), Dhaka-1205, Bangladesh
[e] Department of Applied Chemistry & Chemical Engineering, Dhaka University, Dhaka-1000, Bangladesh

electronics, and magnetic refrigerants due to their low production cost, easy production, and fast production rate.[1–7] These spinel ferrite materials have high coercivity, significant magnetization values, high magnetic characteristics, mechanical hardness, large magnetostrictive coefficient and outstanding chemical and thermal stability.[8–11]

The magnetic properties of cobalt ferrite NPs are significantly influenced by their shape, size and purity, which are determined by the initial conditions used in their production process and thus impact the material's microstructure.[12] Adding cobalt ions to ferrite produces better coercivity because of increased magneto-crystalline anisotropy, which happens due to the spin coupling of the iron and cobalt ions.[13] Among different spinel ferrite compounds, these $CoFe_2O_4$ nanoparticles have an inverse spinel structure with Co^{2+} ions in the octahedral lattice position but the Fe^{3+} ions are positioned differently with half of them in the tetrahedral sites and the rest at the octahedral sites.[14] They are found to be amazing dielectric materials and thus can be used in many applications using microwave to radio frequency. These nanoparticles show cationic inversion as the Fe^{3+} and Co^{2+} distribution is changed among the tetrahedral and octahedral sites. This affects the properties of cobalt ferrite NPs in applications like biomedical imaging, computer tomography (CT scan), magnetic data storage, targeted drug delivery for tumor treatment and microwave devices.[15]

Cobalt is responsible for the emission of gamma rays, which are used in radiation therapy to treat cancer, and it can also be used to sterilize medical implants like syringes and for manufacturing plastics. Also, it is used for sterilizing food to kill bacteria and increase the shelf-life of food. It also helps to reduce the rate of ripening of fruits and prevent sprouting of potatoes and onions.[16] In an antimicrobial study conducted by Gole *et al.*, it was found to be more effective against *S. aureus* than the ciprofloxacin drug and it also showed antifungal activity against *Candida albicans* and *Rhizopus orzae*.[17] In another study conducted by Zhang *et al.*, the sensing of bimetallic oxides was explored and cobalt ferrite, due to its variable polyvalent cations, has been shown to be a potential candidate towards acetone gas sensing.[18] Cobalt ferrite is also used with biochar in carbon paste electrodes and Souza *et al.* have found it to be effective in voltammetric detection of paracetamol in synthetic urine.[19] Cardoso *et al.* successfully removed 93% of phosphorus at 60 °C at pH 6 using cobalt ferrite nanoparticles, showing their effectiveness in effluent treatment, and they are a cheaper and environment friendly option.[20] Cobalt ferrite nanoparticle catalysts have good catalytic efficiency and can be retrieved magnetically as shown by Bekhit *et al.*[21]

There are numerous techniques used to form cobalt ferrite nanoparticles like co-precipitation,[22] solvothermal synthesis,[23] sol–gel methods,[24] reverse micelle approaches,[25] electrochemical methods,[26] microwave-assisted synthesis,[27] combustion methods,[28] or micro-emulsion methods.[29] The sol–gel method is technically one of the most versatile and widely used methods for producing cobalt ferrite nanoparticles. This is advantageous due to low cost and reduced processing temperatures and it has the ability to achieve high-purity and also modify the crystallite size and shape.[30] In the sol–gel method, the metal precursors such as alkoxides or salts undergo hydrolysis reaction and then calcination to produce the final cobalt ferrite nanoparticles. The hydrolysis facilitates the formation of hydroxyl groups (M–OH), which then condense into robust metal–oxo–metal bridges (M–O–M).[31] The reaction conditions such as the concentration of the metal precursor, pH and the calcination temperature can modify the structural and magnetic characteristics of the resulting nanoparticles. This method ensures the desired stoichiometry and provides superior control over phase formation, as well as homogeneity in particle size.[32]

The chemical and physical properties of nanomaterials are influenced by the synthesis technique, as mentioned by several researchers.[33,34] Ivanova *et al.* investigated the impact of annealing temperature on the magnetic characteristics of iron doped cobalt oxide nanoparticles produced by the combustion method and found that increasing the annealing temperature to 800 °C from 400 °C decreased the Congo red dye adsorption capacity of the nanoparticles by half.[35] The author observed that the crystallite size of the nano-particles increased as the annealing temperature increased, and there were notable changes in other physical attributes with increase in magnetization properties. According to Swatsitang *et al.* the average crystal size increases from 80 to 103 nm as the annealing temperature increases when the cobalt ferrite nanoparticles are produced using the polymer pyrolysis technique.[36] Thus, all these studies show that the characteristics of cobalt ferrite nanoparticles can be changed by many factors such as stabilization energy, specific ionic radii, synthesis method, annealing temperature and synthesis conditions.[37]

In this study, the effects of different calcination temperatures on the synthesis of cobalt ferrite nanoparticles through the sol–gel method and on the structural, magnetic, optical or dielectric properties of the nanoparticles are studied. The temperature range of 500 °C to 1000 °C is used because important phase changes like the formation of a spinel phase, enhancement in grain size and variations in properties like conductivity take place in this range. Temperatures below 500 °C produce less well crystallized particles and the temperatures above 1000 °C cause excessive grain growth or the sintering effect. This temperature range allows cobalt ferrite to meet the thermal requirements for applications in magnetic data storage, photocatalysis, MRI, and other fields. Thus, this research focuses on optimizing the sol–gel process to synthesize nanoparticles with better characteristics while keeping the pH value of the preparation solution constant throughout the synthesis process.

2 Experimental

2.1. Chemicals and materials

Cobalt nitrate $[Co(NO_3)_2·6H_2O]$, ferric nitrate $[Fe(NO_3)_3·9H_2O]$, citric acid $(C_6H_8O_7·H_2O)$, glycerol $(C_3H_8O_3)$, and ammonium

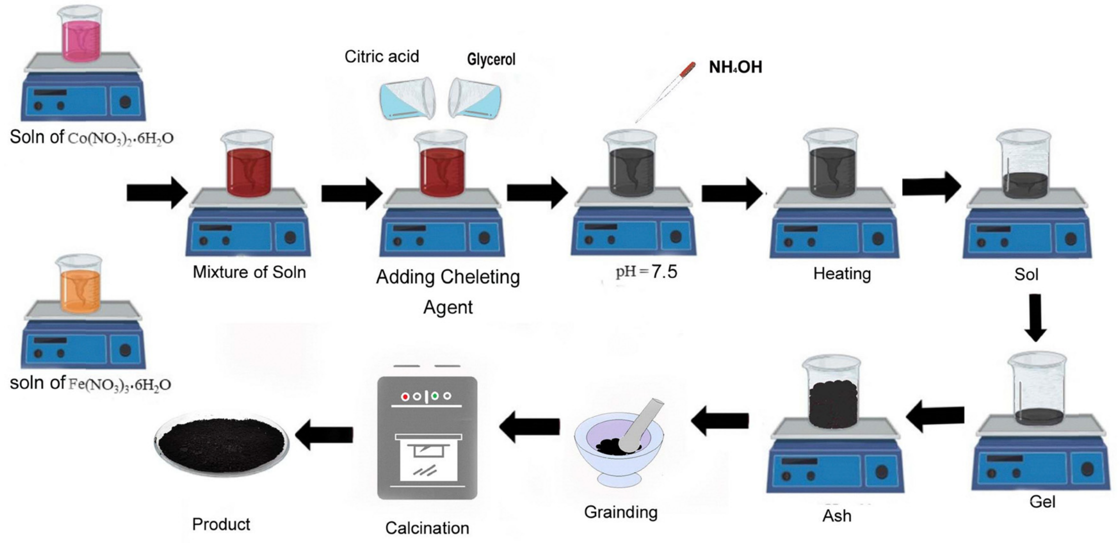

Fig. 1 A schematic diagram showing the preparation of cobalt ferrite nanoparticles by a sol–gel method (at different calcination temperatures).

hydroxide (NH_4OH) used in this experiment were from Merck KgaA, Germany and were of analytical grade. Deionized distilled water is also used in this experiment.

2.2. Synthesis of cobalt ferrite by a sol–gel method (at different calcination temperatures)

Cobalt ferrite nanoparticles were synthesized by using the aqueous solutions, including highly pure salts of cobalt nitrate [$Co(NO_3)_2 \cdot 6H_2O$] and ferric nitrate [$Fe(NO_3)_3 \cdot 9H_2O$] with the molar ratio of 1 : 2, which were stirred for 30 minutes at 40 °C. A mixture of the chelating agent citric acid and the dispersant glycerol with a molar ratio of 1 : 1 was added into the above solution and the precursor solution was heated for 1 hour with magnetic stirring. An ammonia solution was added dropwise to adjust the pH value to ~7.50 and the mixed solution was then allowed to evaporate at 85 °C on a hotplate with continuous stirring until a highly viscous gel was formed. After the formation of the viscous gel, waited for for the formation of ash. Then the ash was placed in an oven at 110 °C for 5 hours and a black precursor was obtained. Finally, the resulting powder was calcined at desired temperatures of 500 °C, 600 °C, 700 °C, 800 °C, 900 °C and 1000 °C in a furnace for 4 hours at the heating rate of 5 °C min^{-1} to obtain black $CoFe_2O_4$ NPs. The obtained black $CoFe_2O_4$ nanoparticle (NP) samples were denoted as T1, T2, T3, T4, T5 and T6 for 500 °C, 600 °C, 700 °C, 800 °C, 900 °C and 1000 °C respectively. This process is demonstrated in Fig. 1.

2.3. Characterization of synthesized cobalt ferrite at different calcination temperatures by a sol–gel method

Using Cu-Kα radiation (λ = 1.5406 Å), the X-ray powder diffraction (XRD) data were found using a scan speed of 10 min^{-1} at 10° ≤ 2θ ≤ 90°. The model of the XRD machine is Smart Lab SE, Rigaku, Japan. Fourier transform infrared (FTIR) spectra were taken between 4000 and 400 cm^{-1} using an IRAffinity-IS, MIRacle 10, Shimadzu, Japan model. Simultaneous thermal analysis (STA) with the model NETZSCH STA 449 F5 was utilized for TGA and DSC analysis at a heating rate of 10 K min^{-1} in a nitrogen atmosphere. UV-visible spectroscopy with the model PerkinElmer Lambda 1050+ was used to find out about the CFOs' optical features and band gap energies in solid powder forms. The vibrating sample magnetometer (VSM) was used to determine the magnetism of the nanoparticles at room temperature.

3 Results and discussion

3.1. X-ray diffraction analysis (XRD)

By utilizing Cu-Kα radiation (λ = 1.5406 Å) with a scan speed of 10° min^{-1} in the range of 10° ≤ 2θ ≤ 90°, an X-ray diffractometer (Smart Lab SE, Rigaku, Japan) was used to examine the phase composition of synthetic $CoFe_2O_4$. Synthesized and calcined CFO nanoparticles' XRD patterns for 500, 600, 700, 800, 900 and 1000 °C are depicted in Fig. 2. The lack of peaks for the as-synthesized sample indicates that calcination is necessary to stabilize the size of crystallites and avoid their aggregation. The 2θ peaks corresponding to reflection planes (1 1 1), (2 2 0), (3 1 1), (2 2 2), (4 0 0), (5 1 1), (4 4 0), and (6 2 0) are visible in the X-ray diffraction patterns of all the calcined samples, verifying that the solitary spinel phase is present. The acquired XRD peaks match the $CoFe_2O_4$ standard pattern described in JCPDS card no. 00-066-0244 rather well. These reflections are part of a fcc type cubic structure.[24]

The Debye–Scherrer and Wilson method, the Williamson–Hall method, the Halder–Wagner method, and the size-strain plot method are all used to calculate the average crystallite size.

The results show that, with the increase of calcination temperature, the diffraction peaks become sharper and

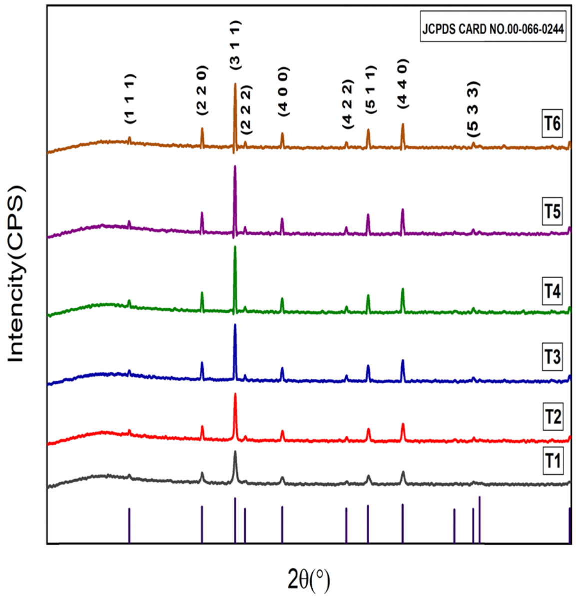

Fig. 2 XRD patterns of CFO nanoparticles calcined at 500 °C, 600 °C, 700 °C, 800 °C, 900 °C and 1000 °C with the standard XRD pattern of CFO.

narrower, and their intensity increases, which confirms that the variation of the calcination temperature has a significant effect on the phase and stoichiometry of the prepared $CoFe_2O_4$ nanoparticles.

3.1.1. Lattice strain and crystallite size estimation

3.1.1.1 The Debye–Scherrer and Wilson (D–S and W) method. The Debye–Scherrer equation was developed to calculate the nanocrystallite size (D) by XRD radiation of wavelength λ (nm) by measuring full width at half maximum of peaks (β) in radians located at any 2θ in the pattern.

$$D_{\mathrm{D-S}} = \frac{K\lambda}{\beta\cos\theta} \qquad \text{(i)}$$

Eqn (i) is the Debye–Scherrer equation, where K represents the Scherrer constant (0.98).[38] Again the following relationship can be used to fix this instrumental broadening:

$$\beta_{\mathrm{d}}^{2} = \beta_{\mathrm{m}}^{2} - \beta_{\mathrm{i}}^{2} \qquad \text{(ii)}$$

where β_{i} is the instrumental widening, β_{d} is the corrected broadening, and β_{m} is the measured broadening. For the sake of this computation of instrumental broadening and position calibration, crystalline silicon has been employed as a standard reference material. Full width at half maximum (FWHM) measurements have been performed to determine the instrumental and physical widening of the sample.[39]

By rearranging eqn (i), the internal breadth may be calculated,

$$\beta = \frac{K\lambda}{\cos\theta \cdot D_{\mathrm{D-S}}} \quad \text{det} \qquad \text{(iii)}$$

If lattice strain is represented by $\varepsilon_{\mathrm{strain}}$ and internal breadth for the strain effect is denoted by β_{strain}, the sample's lattice strain may be determined using the Stokes and Wilson equation in ref. 40,

$$\varepsilon = \frac{\beta_{\mathrm{strain}}}{4\tan\theta} \qquad \text{(iv)}$$

The Debye–Scherrer method for calculating the crystallite size employs a single peak to compute the average crystallite size, which ranges from 24.52 to 148.144 nm. Estimating the average crystallite size may contain some mistake and comparable sorts of inaccuracies are explored in the literature.

The values of average crystallite size ($D_{\mathrm{D\text{-}S}}$) and lattice strain (ε) are given in Table 1.

3.1.1.2. Williamson–Hall (W–H) method. Crystallites with a size (D) of less than or equal to 1 μm show profile widening. Through the so-called Scherrer equation, the integral breadth (in radians), β_D, caused by the influence of tiny crystallites, is related to D[41]

$$\beta_D = \frac{K\lambda}{D\cos\theta} \qquad \text{(v)}$$

By varying Bragg's law, it is possible to determine how isotropic microstrain affects profile broadening.

$$\lambda = 2d\sin\theta \qquad \text{(vi)}$$

Williamson and Hall[42] suggested a simple approximation that the integral width, β, due to both small crystallite sizes and micro-strains is just the sum of the Lorentzian, β_D and Gaussian, β_ε components:

$$\beta = \beta_D + \beta_\varepsilon \qquad \text{(vii)}$$

According to Stokes and Wilson law[43]

$$\beta_\varepsilon = 4\varepsilon\tan\theta \qquad \text{(viii)}$$

Table 1 The average crystallite size and lattice strain of the cobalt ferrite nano-crystallites (synthesized using the sol–gel method at different calcination temperatures) determined using the Debye–Scherrer and Wilson method, Williamson–Hall method, Halder–Wagner method and size–strain plot

	D–S and Wilson method		Williamson–Hall method		Halder–Wagner method		Size–strain plot technique	
Sample	$D_{\mathrm{D\text{-}S}}$ (nm)	$\varepsilon_{\mathrm{W}} \times 10^{-2}$	$D_{\mathrm{W\text{-}H}}$ (nm)	$\varepsilon_{\mathrm{W\text{-}H}} \times 10^{-4}$	$D_{\mathrm{H\text{-}W}}$ (nm)	$\varepsilon_{\mathrm{H\text{-}W}} \times 10^{-3}$	D_{SSP} (nm)	$\varepsilon_{\mathrm{SSP}}$
T1	24.52	0.41	32.40	10.20	33.52	1.74	4.17	0.75
T2	49.10	0.21	44.15	2.72	41.85	0.58	7.82	0.26
T3	77.49	0.34	95.27	1.48	83.70	0.52	9.52	0.18
T4	117.12	0.09	147.44	1.98	120.68	0.24	15.92	0.12
T5	135.39	0.07	147.80	0.65	150.42	0.24	19.33	0.12
T6	148.14	0.33	152.25	0.01	169.20	0.36	19.59	0.14

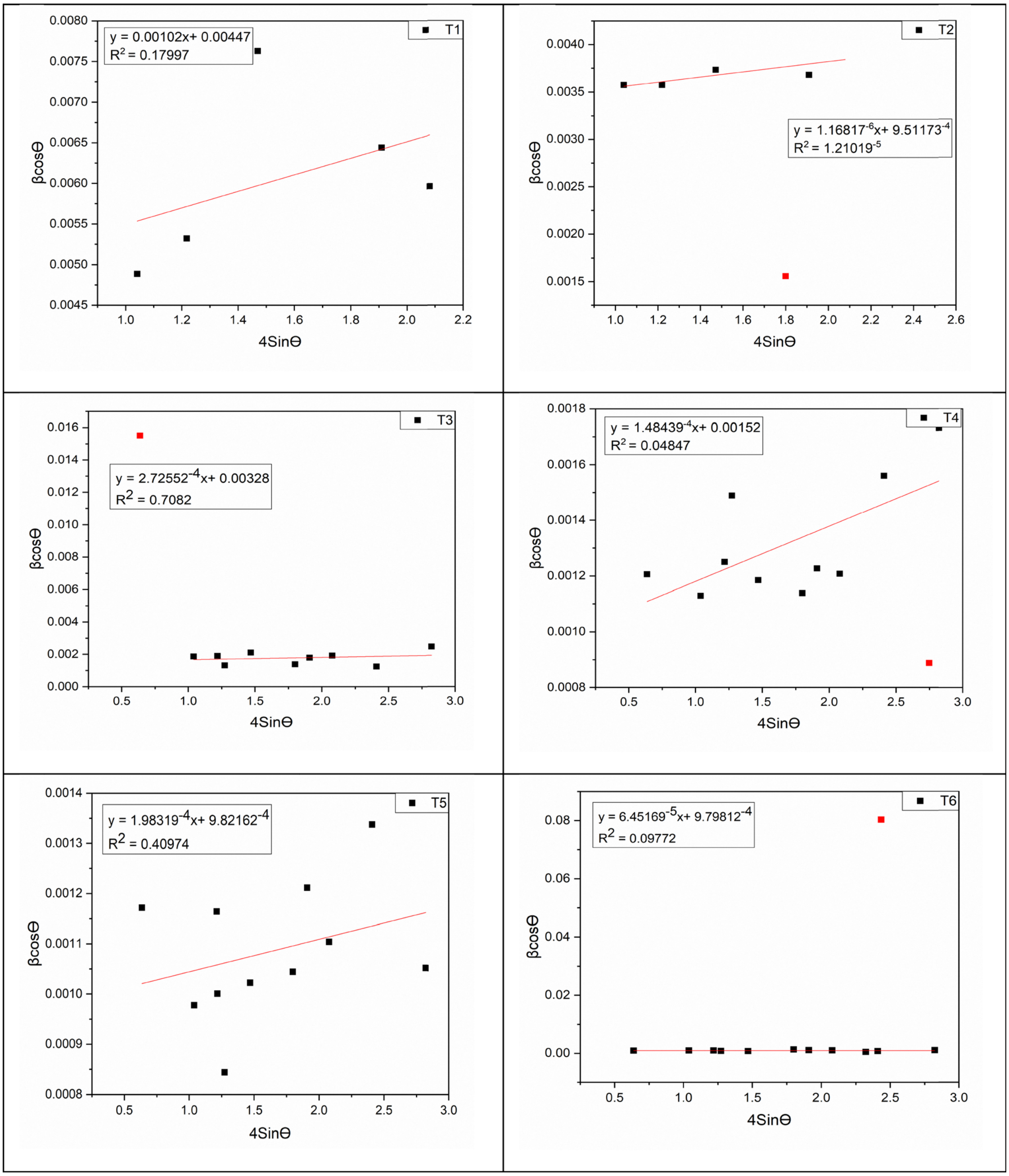

Fig. 3 W–H plot of cobalt ferrite nanoparticles (for different calcination temperatures).

From eqn (v) and (viii) the values of β_D and β_ε are put in eqn (vii),

$$\beta = \frac{K\lambda}{D\cos\theta} + 4\varepsilon\tan\theta \qquad \text{(ix)}$$

or,

$$\beta\cos\theta = 4\varepsilon\sin\theta + \frac{K\lambda}{D} \qquad \text{(x)}$$

Eqn (x), $y = ax + b$, is thought of as a straight line. The Williamson–Hall (WH) plot is a conflict between the equations $y = \beta\cos\theta$ and $x = \sin\theta$ in Fig. 3.

This model was inaccurate since the straight lines that were shown did not produce a good regression co-efficient (R^2 value is low), even though the predicted crystallite sizes ranged from 32.4 to 152.25 nm. The W–H plot does not suit the presented straight lines well, as evidenced by the R^2 correlation coefficient. 0.17997, 1.21019, 0.7082, 0.04847, 0.40974, and 0.09772 are the respective R^2 values of the plotted straight lines according to the W–H method, not good fitted as well.[38]

3.1.1.3. Halder–Wagner (H–W) method. Halder and Wagner[44] developed an alternative equation incorporating the integral width, β^*, of the reciprocal lattice point and the lattice plane

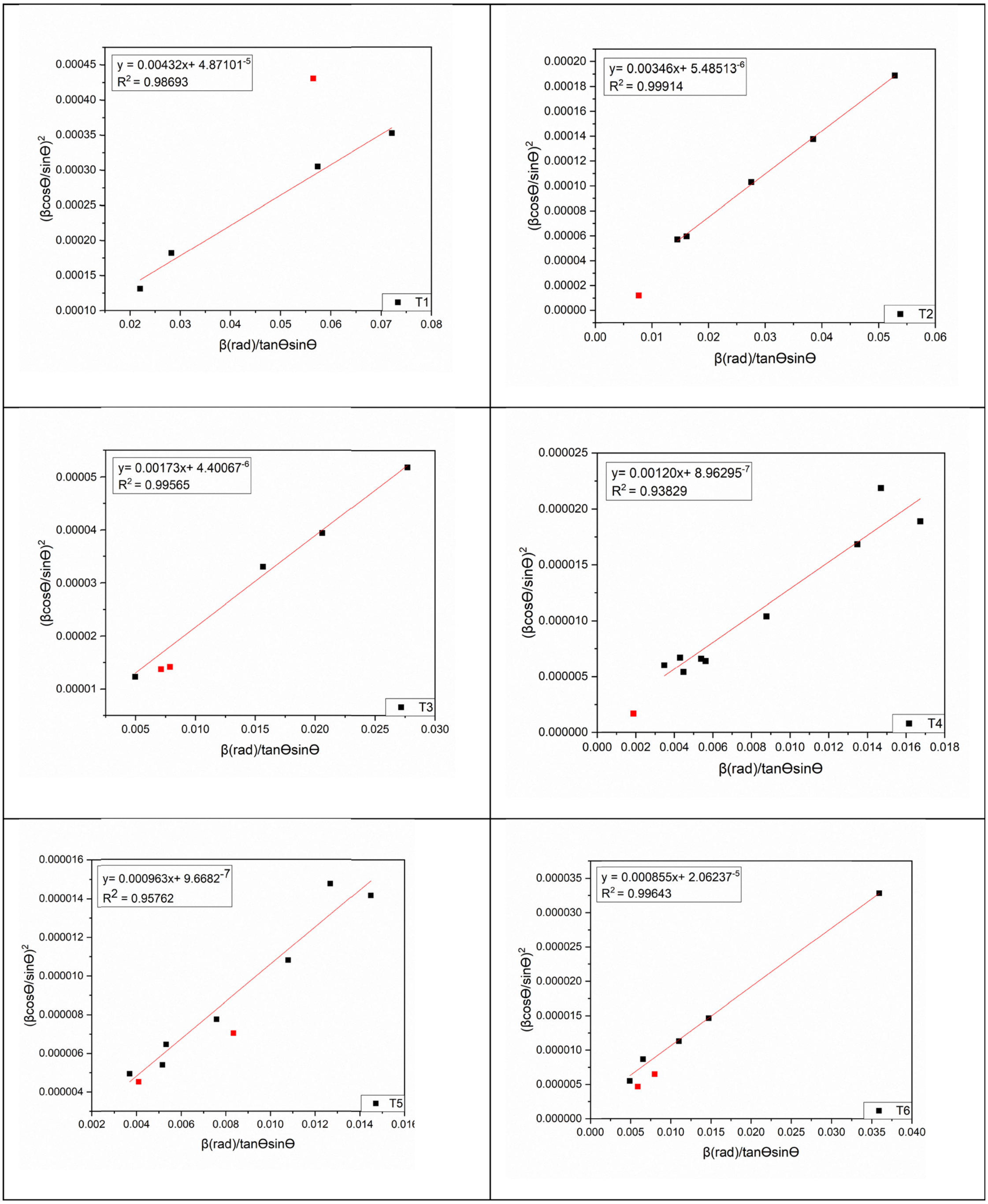

Fig. 4 H–W plot of cobalt ferrite nanoparticles (for different calcination temperatures).

spacing, d^*, for the reciprocal cell to determine D and ε:

$$\left(\frac{\beta^*}{d^*}\right)^2 = \frac{K}{D}\cdot\frac{\beta^*}{(d^*)^2} + (4\varepsilon)^2 \qquad \text{(xi)}$$

with

$$\beta^* = \frac{\beta\cos\theta}{\lambda} \qquad \text{(xii)}$$

and,

$$d^* = \frac{2\sin\theta}{\lambda} \qquad \text{(xiii)}$$

on the grounds that the size and strain effects are the only causes of the Lorentzian and Gaussian components of β^*, respectively. So, eqn (xi) can be rephrased as,

$$\left(\frac{\beta}{\tan\theta}\right)^2 = \frac{K\lambda}{D}\cdot\frac{\beta}{\tan\theta\sin\theta} + 16\varepsilon^2 \qquad \text{(xiv)}$$

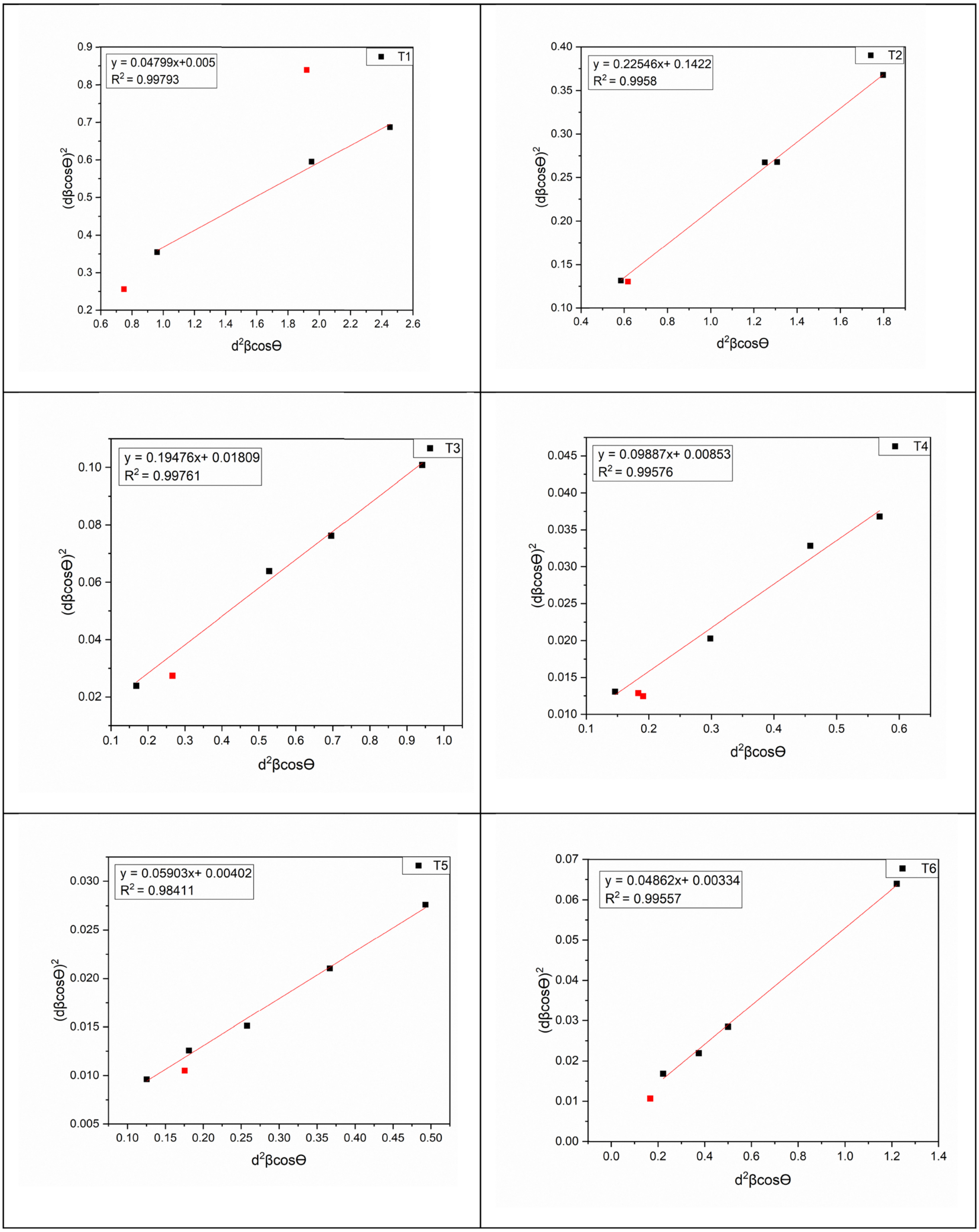

Fig. 5 SSP plot of cobalt ferrite for different calcination temperatures.

or,

$$\left(\frac{\beta\cos\theta}{\sin\theta}\right)^2 = \frac{K\lambda}{D}\cdot\frac{\beta\cos\theta}{\sin^2\theta} + 16\varepsilon^2 \qquad \text{(xv)}$$

Since sin and cos are included in eqn (xv), the corresponding version of eqn (xiv) is selected. Eqn (xiv) is shaped like a straight line, $y = ax + b$. As seen in Fig. 4, the Halder–Wagner (H–W) plot compares $y = (\beta/\tan\theta)^2$ to $x = \beta/(\tan\theta\sin\theta)$. The resulting straight line's slope and y intercept then yield $K\lambda/D$ and $16\varepsilon^2$, respectively. As stated in the preceding section, the value of $K = 4/3$ is thought to be true when the crystallite size is defined as the volume-weighted average for spherical crystallites.

Similar sorts of observations have been reported in the literature.[38] The correlation co-efficient values of R^2 for the straight lines drawn using the H–W approach are 0.98693, 0.99914, 0.99565, 0.93829, 0.95762, and 0.99643, respectively. The correlation coefficient value of R^2 indicates that the straight lines shown using the H–W approach fit the data well.

3.1.1.4. Size–strain plot (SSP) method. The SSP method has the advantage of giving more weight to peaks in the low and intermediate angle ranges since the overlap between the diffraction peaks is significantly less. The Halder–Wagner technique now provides the connection between the crystal size and the lattice strain.[45]

$$\left(\frac{\beta_{hkl}}{d_{hkl}}\right)^2 = \frac{1}{D}\left(\frac{\beta_{hkl}}{d_{hkl}}\right) + \left(\frac{\varepsilon}{2}\right)^2 \qquad \text{(xvi)}$$

The Williamson–Hall approach actually evaluates peak broadening as a function of diffraction angle (2θ), which is supposed to represent a joint effect of size and strain driven broadening. However, there are models that deal with peak profile analysis. One such method is the size–strain plot (SSP), which assumes that the XRD peak profile is a combination of Lorentzian and Gaussian functions, with size broadened XRD profiles labeled as Lorentz functions and strain broadened profiles labeled as Gaussian functions.[46] As a result, the overall broadening of SSP can be written as eqn (vii).

$$\beta = \beta_D + \beta_\varepsilon.$$

Furthermore, the SSP technique always produces a better result for isotropic broadening because it prioritizes low angle reflections, where accuracy and precision are higher, above higher angle reflections. This is due to the decreased quality of XRD data at higher angles, and peaks are often substantially overlapped at higher diffracting angles.

As a result, the SSP calculation is carried out using the equation[47] shown below,

$$(d_{hkl}\cdot\beta_{hkl}\cdot\cos\theta)^2 = \frac{K\lambda}{D}(d_{hkl}{}^2\cdot\beta_{hkl}\cdot\cos\theta) + \frac{\varepsilon^2}{4} \qquad \text{(xvii)}$$

where the (hkl) plane's lattice distance is denoted by the symbol d_{hkl}. Now, using eqn (xvii), the graphs are made with each diffraction peak's ($d_{hkl}{}^2\cdot\beta_{hkl}\cdot\cos\theta$) term along the X-axis and $(d_{hkl}\cdot\beta_{hkl}\cdot\cos\theta)^2$ along the Y-axis, as shown in Fig. 5. The average sizes are given as 4.17 to 19.59 nm by the straight line's slope.

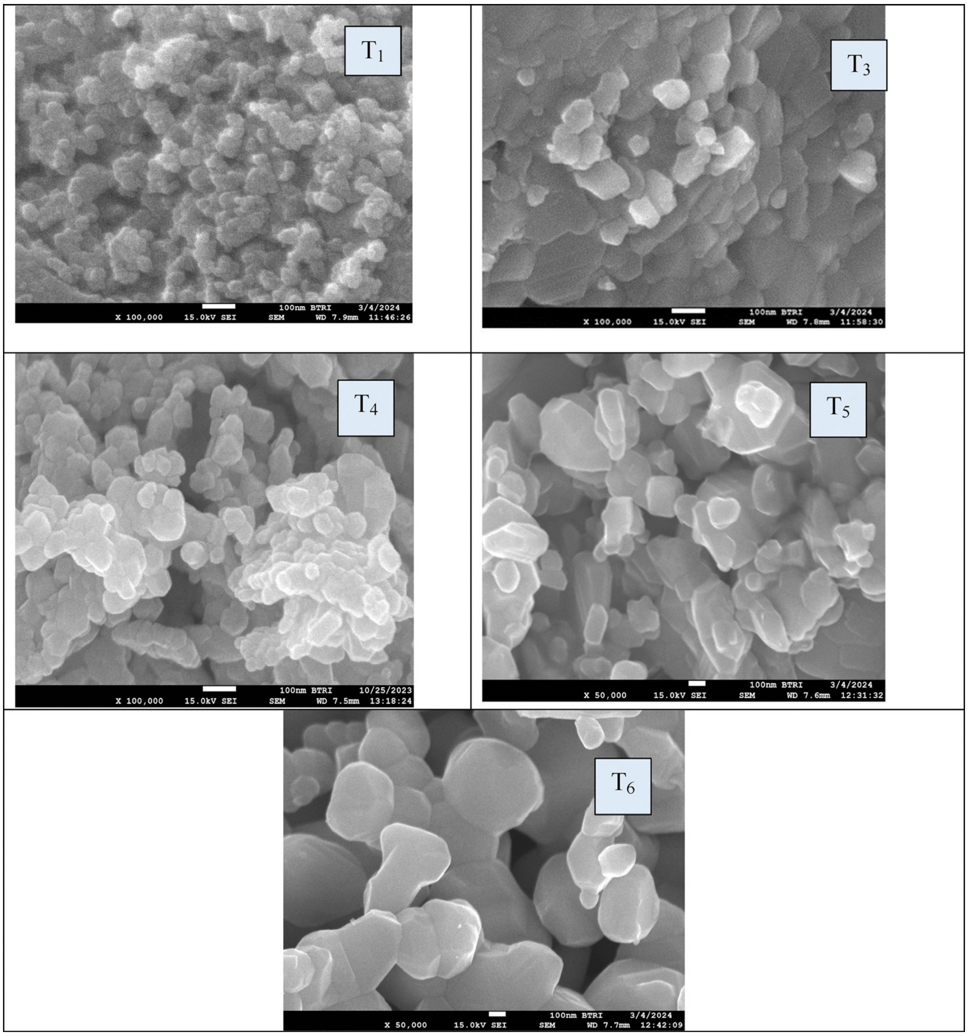

Fig. 6 SEM micrographs of the $CoFe_2O_4$ sample.

The correlation coefficient values of R^2 for the straight lines plotted using the SSP approach are 0.99693, 0.99580, 0.99761, 0.99576, 0.98411, and 0.99557, respectively and the correlation coefficient value of R^2 indicates that the straight lines plotted using the SSP approach are well fitted.

The results obtained for structural parameters are quite similar for SSP and H–W plots and the data are more accurately fit in both these methods with all high intensity points touching linear adaptation. So, it is clear that SSP and H–W methods are the best methods. The values of the crystallite size for different metal ion concentrations of $CoFe_2O_4$ nanoparticles synthesized using different methods are more or less similar. Different analytical methods like Debye–Scherrer, Williamson–Hall, Halder–Wagner, and size–strain plots are used to check and cross-check the estimation of the crystallite size and contribution of strain and instrumental broadening and the values are not necessarily similar but they all follow the same pattern that as calcination temperature increases the crystal size also increases. Different methods use different positions of crystals and the size and shape of the crystals vary with crystal strength and thus using multiple methods gives a better understanding of the whole picture. Also, different methods have different advantages and assumptions like Debye–Scherrer assumes strain almost negligible but Williamson–Hall and Halder–Wagner include strain effects and the lattice distortions observed at higher calcination temperatures. The size–strain plot (SSP), which separates the size and strain effects, yields the most reliable values. Table 1 tabulates the strain and the nanoparticle crystal size data for the Debye–Scherrer and Wilson method, Williamson–Hall method, Halder–Wagner method and size–strain plot. It also shows that as the calcination temperature is increased, the size of the crystals of cobalt ferrite nanoparticles is also increased.

3.2. Morphological analysis

SEM micrographs of the $CoFe_2O_4$ sample annealed at 500 °C, 600 °C, 700 °C, 800 °C, 900 °C and 1000 °C are shown in Fig. 6. It shows that the majority of the particles have nearly spherical morphology. The particles are homogeneously distributed, and their size is non-uniform. The average size of the particles for each sample has been estimated by fitting the particle size distribution histogram to the log-normal distribution function, which is represented as[48]

$$f(D) = \left(\frac{1}{\sqrt{2\pi}\sigma_D}\right)\exp\left[-\frac{\ln^2\left(\dfrac{D}{D_0}\right)}{2\sigma^2}\right]$$

where D corresponds to the average particle size and σ_D is the standard deviation. The estimated average particle size for the 800 °C annealed sample is found to be 46.72 nm along with a standard deviation of 1.16 nm. The particles of the sample annealed within 500–1000 °C falls in the nanometer range, which will be near to the average crystallite size estimated by the XRD study. Table 2 shows the average particle size and the standard deviation of the samples as estimated from the SEM image using ImageJ software.

Table 2 Average particle size estimation from SEM analysis

Sample name	Synthesis temperature (°C)	Average particle size (nm)	Standard deviation (σ_D)
T1	500	45.45	1.91
T3	700	73.64	3.70
T4	800	46.72	1.16
T5	900	136.23	7.30
T6	1000	349.97	6.28

The possible explanation for the increase of the particle size with annealing temperature is as follows: smaller particles possess a big surface area. Upon increasing the annealing temperature, a number of nearby particles fuse together to agglomerate *via* surface melting. As a result, the size of the particles becomes large.

3.3. Magnetic properties of $CoFe_2O_4$

The magnetic properties of the $CoFe_2O_4$ nanoparticles calcined at 500 °C, 600 °C, 700 °C, 800 °C, 900 °C and 1000 °C were examined by vibrating sample magnetometer (VSM) analysis. From the VSM measurements, the magnetization and coercivity values with respect to the magnetic field are shown in Fig. 7 for the $CoFe_2O_4$ samples measured at room temperature, revealing the ferromagnetic behavior. This sort of behavior will be influenced by cobalt ferrite's high magneto-crystalline anisotropy.[49]

With a view to assess the magnetic behavior of the cobalt ferrite nanoparticles, the recorded hysteresis loops of all the samples at ambient temperature using a vibrating sample magnetometer are presented in Fig. 7. From the hysteresis loops, various magnetic parameters *viz.*, saturation magnetization (M_s), coercive field (H_c) and reduced remnant magnetization ($R = M_r/M_s$) are evaluated and presented in Table 3. The non-zero value of remnant magnetization, M_r, and a

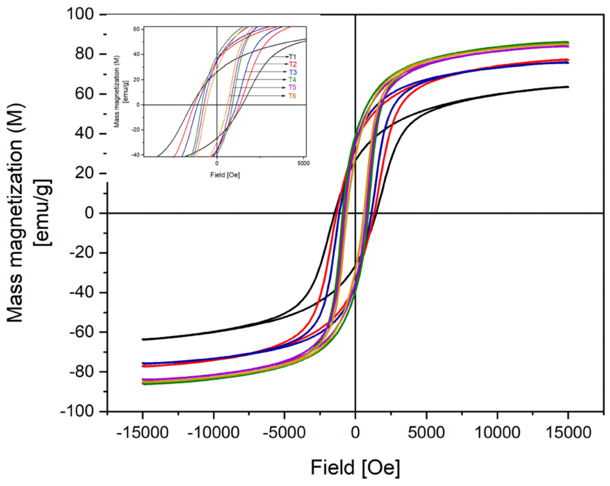

Fig. 7 *M*–*H* curves measured at room temperature for $CoFe_2O_4$ samples calcined at various temperatures.

Table 3 The values of saturation magnetization (M_s), retentivity (M_r), coercivity (H_c), magnetic anisotropy (K) and rectangular ratio (R_s) for T1, T2, T3, T4, T5 and T6

	Saturation magnetization	Remnant magnetization	Coercivity	Magnetic anisotropy	Reduced remnant magnetization
Sample	M_s	M_r	H_c	$K = (M_s \times H_c)/0.96$	$R_s = M_r/M_s$
T1	62.00	26.00	1460.00	1679.16	0.42
T2	76.00	35.00	1319.00	2770.83	0.46
T3	74.00	36.00	1122.00	2775.00	0.48
T4	85.00	39.00	889.00	3453.13	0.45
T5	83.00	34.00	757.00	2939.58	0.41
T6	84.00	28.00	609.00	2450.00	0.33

considerably high value of H_c are the general characteristics of hard ferro- or ferri-magnetic materials.[50]

Samples suggest that the developed cobalt ferrite nanoparticles fall under the above-mentioned categories. Moreover, decrease of H_c with increase of calcination temperature is also observed. The maximum value of H_c is found to be 1460 Oe for the temp. 500 °C. For the cobalt ferrite nanoparticles of still higher dimensions, the value of H_c is found to be lower. Upon heating at 500 °C, the smaller particles should be single domain particles with high anisotropy. The bigger particles for T4, T5, and T6 will start behaving like multi-domain particles. The coercivity of the bigger particle will be lower as it becomes multi-domain. The Stoner–Wohlfarth model supports the idea that as the particle size becomes larger domain wall motion plays a significant role in coercivity.[51] To be mentioned in detail, for the nanoparticles of the average temp. 800 °C, the value of M_s is extraordinary higher (85 emu g^{-1}) and the corresponding coercive field is found to be 889 Oe (Table 3). This falls in line proving the high crystallinity and larger particle sizes confirmed by XRD and SEM, respectively, reducing surface spin disorder and improving the alignment of the magnet.[52] The inference of this behavior is that there is a transition of the state of the material from low temp. to high temp. Above 800 °C, there is a slight decrease in saturation magnetization, which is attributed to excessive grain growth or partial cation migration disrupting optimal spin alignment of Fe^{3+}/Co^{2+}.[53] At higher temperature, the Co^{2+} ions move from octahedral sites to tetrahedral locations, which changes the net magnetization. To throw more light on the magnetic characteristics of the studied samples, the magneto-crystalline anisotropy constant, K, using the Stoner–Wohlfarth relation has been evaluated for the cobalt ferrite nanoparticles annealed at different temperatures. The value of K is observed to increase with the particle size. The maximum value of K for the sample with the temp. of 800 °C is estimated to be 3.4×10^6 erg cm^{-3} (Table 3); this value of K is nearly equal to that of the bulk single phase $CoFe_2O_4$ reported by other authors, due to optimal Co^{2+} occupancy in octahedral sites enhancing spin–orbit coupling. Furthermore, it may be noted here that with the decrease of temperature (from 800 °C) the value of K is found to decrease rather than remaining invariant as reported earlier. This shift in intrinsic magnetic anisotropy is caused by differences in (i) the particle size, (ii) the particle shape, and (iii) interparticle interactions.

The theoretical value of M_r/M_s for non-interacting uniaxial single domain particles with a randomly oriented easy axis is 0.5, according to the Stoner Wohlfarth model.[54] The observed M_r/M_s values for the pure samples T1, T2, T3, T4, T5, and T6 are 0.42, 0.46, 0.48, 0.45, 0.41 and 0.33 respectively. As a result, CFO displays uniaxial anisotropy. The optimum temperature for achieving the peak of magnetic saturation and anisotropy is 800 °C. The c and domain structure at this temperature will provide high magnetization and moderate coercivity. Magnetic storage applications will benefit from this property. Also, lower temperatures favor applications needing high coercivity while higher temperatures are good for soft magnetic materials.[55]

3.4. Fourier transform infrared (FTIR) analysis

The presence of functional groups (metal–oxygen bonding) and impurities on the surface of the prepared samples was investigated using Fourier transform infrared (FT-IR) analysis, where the IR absorption bands of solid matrices are typically attributed to the vibration of ions in the crystal lattice. The main vibrational modes of metal–oxygen (M–O) bonds, which correspond to metals in a tetrahedral or octahedral configuration for spinel structures, are depicted in Fig. 8 between 300 and 670 cm^{-1}. Bands of M–O bonds typically develop in octahedral sites between 380 and 450 cm^{-1}, whereas they do so in tetrahedral sites between 540 and 600 cm^{-1}.[56]

In this instance, the presence of the $CoFe_2O_4$ spinel was indicated by a band of M–O bonds at the octahedral sites, which appeared at 402–403 cm^{-1}, and the band at the tetrahedral sites appeared at 576–580 cm^{-1}.[57] Besides, the vibration at 470 cm^{-1} indicates the band of Co–OH.[58] The vibrational modes of the absorbed water molecules' –OH stretching and bending are responsible for the broad bands near 3462 and 1630 cm^{-1}, respectively.[59] Little peaks are produced at around 2925 cm^{-1} by the C–H stretching vibration. A small peak at 1400 cm^{-1} is caused by residual nitrogen groups from the combustion event, whilst the absorption band caused by CO_2 is at 2350 cm^{-1}.[60] Each sample's vibrational modes revealed the presence of spinel $CoFe_2O_4$.

3.5. Thermal analysis

The thermal stability of CFO nanoparticles was explored by using a NETZSCH STA 449 F5 simultaneous thermal analyzer (STA). In Fig. 9 the TGA curve shows six stages of weight loss,

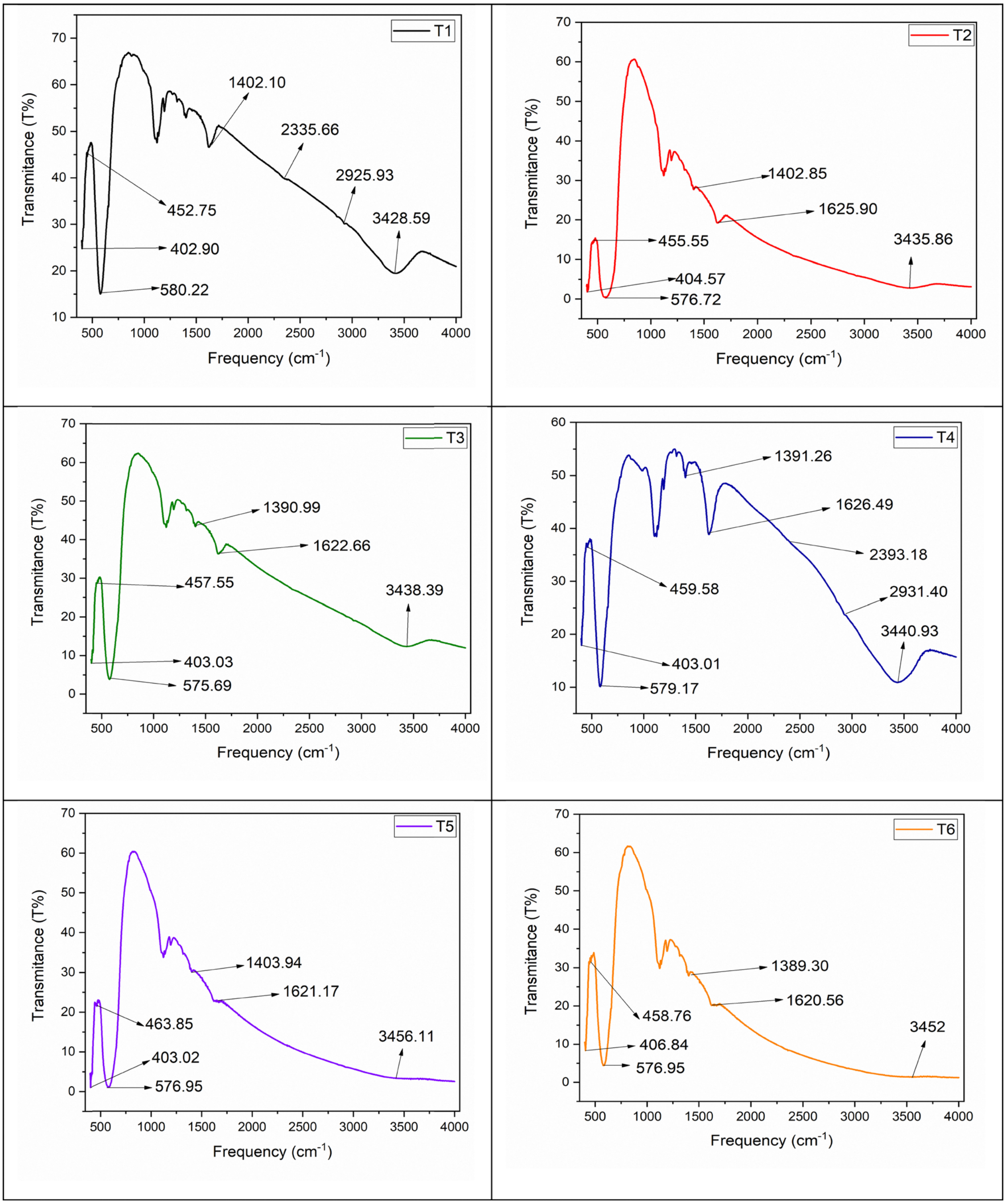

Fig. 8 FT-IR spectra of T1, T2, T3, T4, T5 and T6.

while the DSC curve shows five exothermic peaks and an endothermic peak. First, it is evident that as water evaporates from ambient temperature to 143 °C, 3.27% of its weight is lost. Furthermore, 4.54% of the weight is lost due to the evaporation of the remaining moisture up to 162 °C. which is related to an exothermic sharp peak around 156 °C in the DSC curve.[61] The third weight loss occurs at 160 to 240 °C due to the decomposition of the functional groups of citric acid and glycerol, which corresponds to the exothermic peak obtained at a temperature of 200 °C in the DSC curve. The highest (21.39%) weight loss was observed for organic matter and nitrogen compound's combustion in the fourth stage from 242 to 475 °C. Finally, 8.52% weight loss occurred for the development of nanoparticles at up to 586 °C, which is related to the sharpest exothermic peak in the DSC curve at 590 °C.[62] And the last 7.44% weight loss occurs due to other internal reactions.[63]

$$\mathrm{Fe(NO_3)_3{\cdot}9H_2O + Co(NO_3)_2{\cdot}6H_2O + C_6H_8O_7 + C_3H_8O_3} \\ \rightarrow \mathrm{CoFe_2O_4 + CO_2 + H_2O + N_2 + O_2}$$

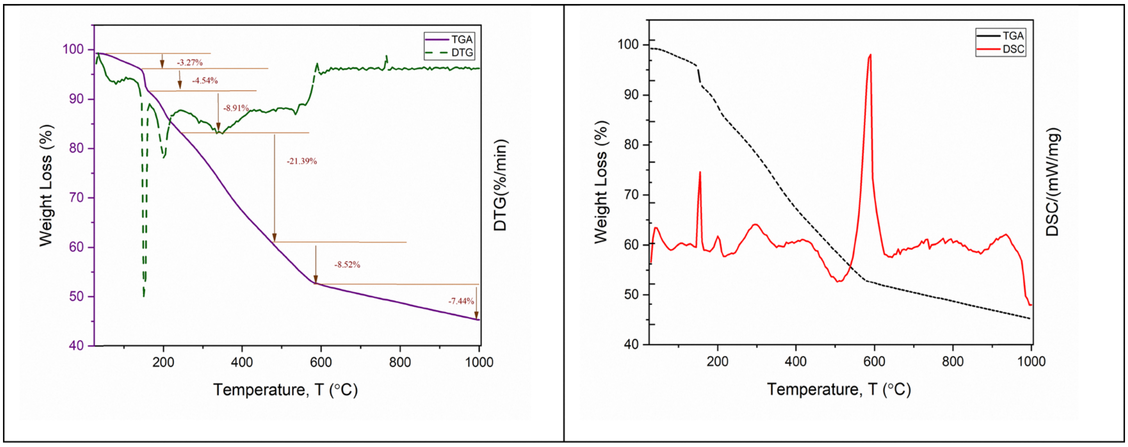

(a) (b)

Fig. 9 Thermal behavior of the $CoFe_2O_4$ sample before calcination (for the sol gel method) (a) DTG and (b) DSC.

3.6. Dielectric properties

The formula was used to find the cobalt ferrite's dielectric constant,

$$\varepsilon' = \frac{Cd}{\varepsilon_0 A}$$

where A is the cross-sectional area of the flat surface of the pellets in meter square, ε_0 is the permittivity of free space, and C is the capacitance of the pellets. Fig. 10 shows the dielectric constant *versus* frequency curves. In all samples, the dielectric constant drops with increasing frequency. The dielectric constant (ε') decreases at higher temperature from around 1.1×10^7 for T1 to around 0.5×10^6 for T6 due to reduced grain boundary density, as coalesced grains minimize interfacial polarization. Higher calcination temperature for T4, T5, and T6 causes more grain growth and coalescence, which reduces grain boundary density. Thus, the total interfacial polarization sites are reduced, which is why the dielectric constant decreases as temperature increases.[64] When the temperature of calcination is lower, the structural defects, oxygen vacancies and Fe^{2+} ions of the solid samples are in a greater amount. Defects are sites for polarization and at low frequency as charge carriers accumulate at the grain boundaries, which creates space charge polarization, there is high resistivity, which requires a large amount of energy to transfer electrons between Fe^{2+} and Fe^{3+} at the octahedral site.[65] Thus, the dielectric constant increases. Higher calcination temperatures reduce these defects, which causes a decrease in polarization mechanisms, and thus the dielectric constant decreases. As Maxwell–Wagner anticipated, this frequency-dependent behavior is due to interfacial polarization.[66] This model assumes that a ferrite material's dielectric structure is composed of two layers: the grain boundaries, which are poor conductors, and the conductive layer, which is made up of big ferrite grains. As a result of the electron exchange between Fe^{2+} and Fe^{3+}, the electrons are locally displaced in the direction of the applied field, which creates the polarization. The prevalence of species such as Fe^{2+} ions, oxygen vacancies, grain boundary defects, *etc.* could be the cause of the increased dielectric constant value at lower frequencies. Any effect contributing to polarization is seen to show lagging behind the applied field at higher frequencies, making the reduction in the dielectric constant with frequency.

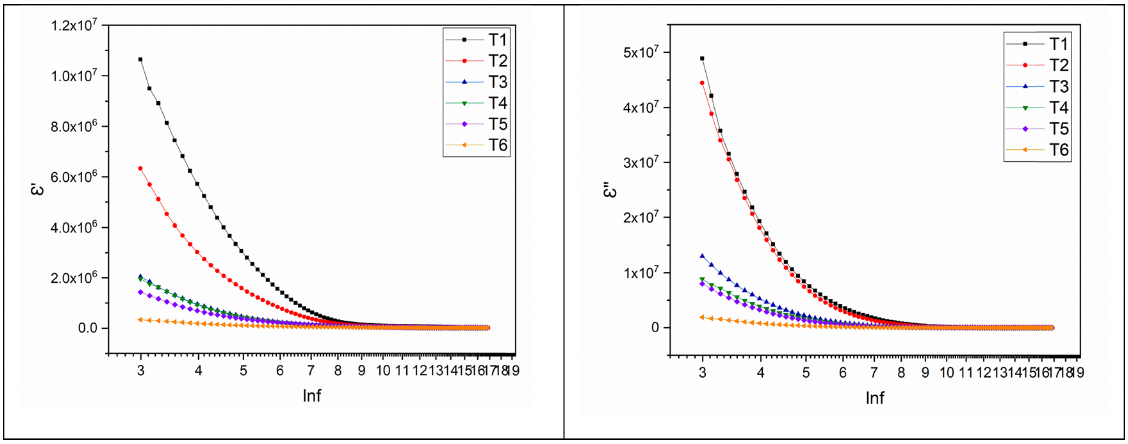

Fig. 10 Dielectric constant (ε' & ε'') behaviour of the samples in the frequency range 20 kHz to 20 MHz.

The dielectric constant decreases as the frequency is raised over a certain point because the electron hopping is unable to follow the variations in the electric field. According to Koop,[67] the grain boundaries, which have a high dielectric constant because of high resistivity there, are where the dielectric constant at low frequency originates. Due to their low resistivity, grains have a small dielectric constant, which is the source of the dielectric constant at high frequencies. It is possible to draw the conclusion that the direction of an electric field, which causes electrical polarization in ferrites, is caused by the exchange of electrons between Fe^{2+} and Fe^{3+} ions. Potential causes of the elevated dielectric constant at low frequencies include flaws, dislocations, and voids. Dielectric loss, $\tan\delta$, is proportional to the loss of energy by means of heat when the electric field is applied and increases with synthesis temperature at low frequencies.[68] Thus, the calcination temperatures can be used for tuning the dielectric properties of CFO nanoparticles, which can be used for enhanced electronic applications.

3.7. Band gap energy analysis

Because electrons are transferred through energy bands, materials often show a considerable increase in light absorption at a specific energy value.[69] The optical absorption spectra of CFO ($CoFe_2O_4$) nanoparticles at ambient temperature were collected in order to determine the band-gap energy of the calcined particles at different temperatures as shown in Fig. 11. In many cases, the direct form is more valuable than the indirect form. All the ferrite compounds' energy band gaps have been computed using the optical absorbance (A) and wavelength (λ) data.

On the other hand, the formula $\alpha = A(h\nu - E_g)^n/h\nu$ represents the relationship between the absorption coefficient (α) and the incident photon frequency (ν), where E_g is the band gap energy and h is the Planck constant. The optical band gap (E_g) is determined from this equation and the value of n is 1/2 for direct transition and direct band gap is estimated using Tauc's model because the cobalt ferrite samples' band structure and optical transitions have been consistently modeled as direct in many studies especially in nanocrystalline spinel ferrites.[70,71]

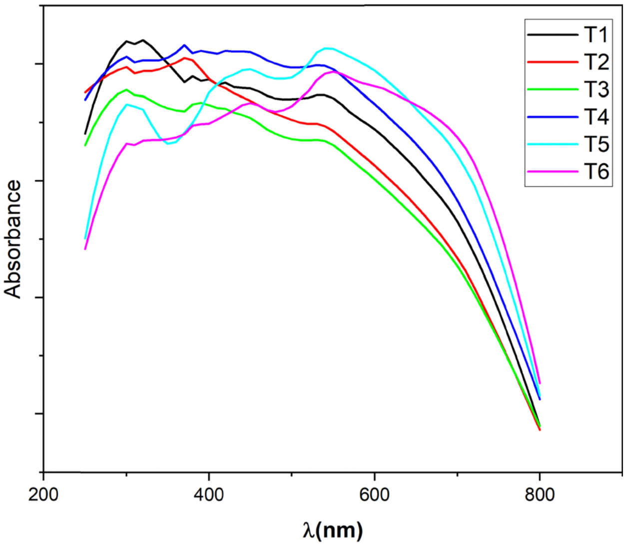

Fig. 11 Absorption spectra of $CoFe_2O_4$ (T1, T2, T3, T4, T5, and T6) nanoparticles in the visible wavelength range.

Table 4 Band gap energy for T1, T2, T3, T4, T5 and T6

Sample	Crystal size (nm)	Band gap energy (eV)
T1	4.17	3.37
T2	4.82	3.10
T3	9.51	3.25
T4	15.92	3.52
T5	19.33	3.00
T6	19.59	3.12

The sol–gel prepared $CoFe_2O_4$ was optically examined at room temperature using the diffuse refraction (R) technique. $(\alpha h\nu)^2$ is plotted in the y-axis and $h\nu$ is plotted in the x-axis. The following formula may be used to calculate α from R,[72]

$$\alpha = \frac{(1-R)^2}{2R}\ (\mathrm{cm}^{-1}) \qquad \text{(xviii)}$$

The band gap energy is determined by the line's intercept at $\alpha = 0$.

The values of the energy band gap for all the samples have been found to be in the range of ~3.00 eV, as listed in Table 4. The direct band gap is found to be 3.10–3.52 eV for as-synthesized CFO nanoparticles,[73] whereas it is 3.37, 3.10, 3.25, 3.25, 3.52, and 3.12 eV for CFO nanoparticles annealed at 500 °C, 600 °C, 700 °C, 800 °C, 900 °C and 1000 °C for 4 hours, respectively (Fig. 12).

3.8. Zeta potential analysis

The zeta potential of the synthesised cobalt ferrite nanoparticles was evaluated using a Zetasizer (SZ-100, HORIBA Scientific Ltd, Japan) in water as a dispersant at neutral pH (~6.20). Fig. 13 shows the distributions of intensity and zeta potential for the six NPs. Table 5 also provides a summary of the values for calcination temp. and zeta potential, where cobalt ferrite samples calcined at 500 °C, 600 °C, 700 °C, 800 °C, 900 °C, and 1000 °C have zeta potentials of −31.9 mV, −45.1 mV, −40.7 mV, −53.3 mV, −50.2 mV, and −61.4 mV respectively. The table shows that the zeta potential value of calcined particles at all temperatures is less than −30 mV. Generally, particles whose zeta potential values are greater than +30 mV and less than −30 mV are considered stable particles.[74] The stability of the solution is improved by proving the repulsion of the particles and achieving a strong negative value for the ferrites at 1000 °C, the calcination temperature. Again, at 500 °C temperature, the value of zeta potential is the lowest (−31.9 mV) and it settles down faster than others due to less electrostatic repulsion present for less negatively charged oxygen ions at the particle surfaces, and thus they are unstable.[75] The T6 particles are much more

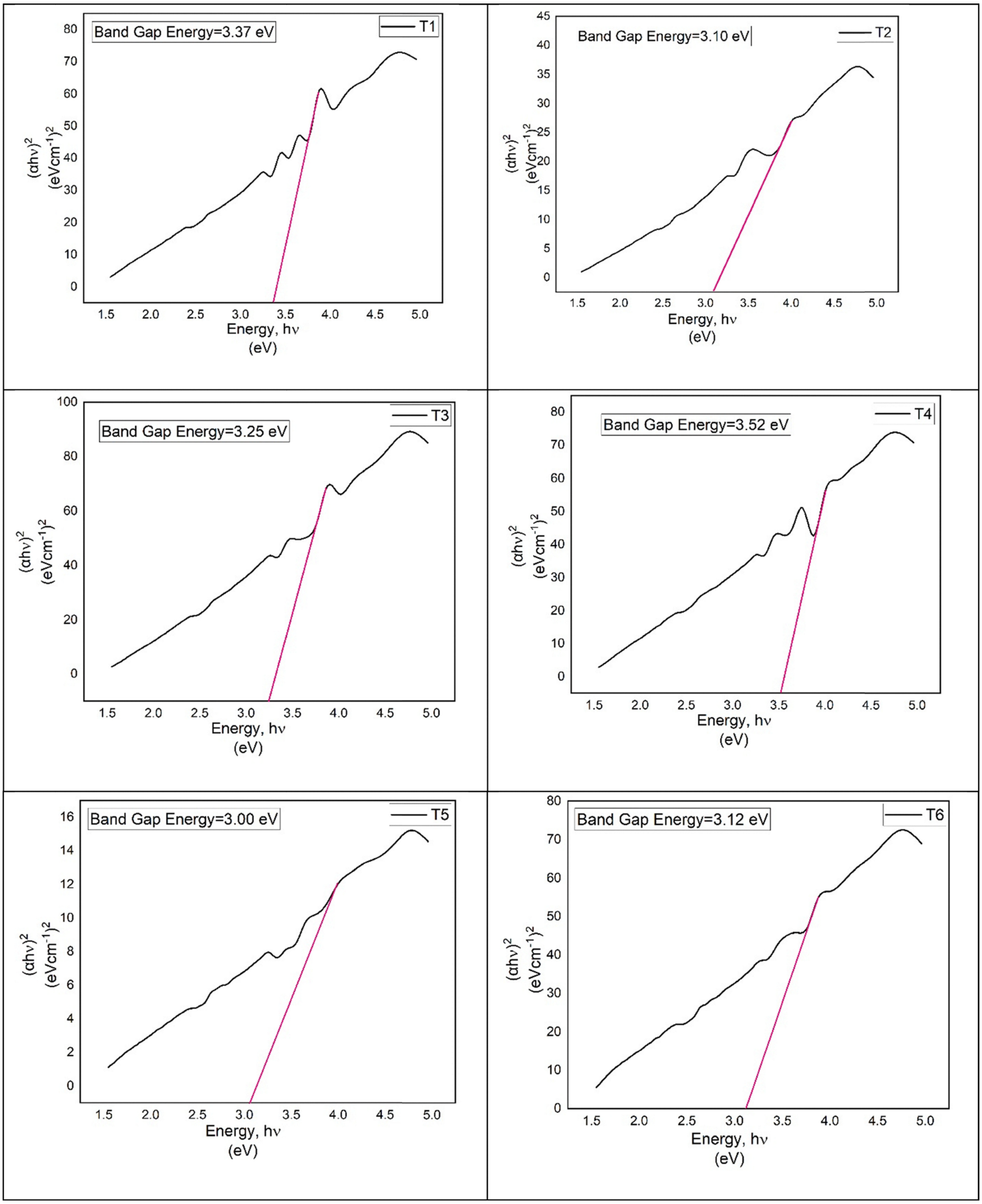

Fig. 12 Band gap energy of cobalt ferrite (CFO) NPs (T1, T2, T3, T4, T5 and T6).

stable in water, which means their shelf-life is larger when suspended in water and will not agglomerate over a long period compared with the other samples. Due to their strong negative charges these nanoparticles exhibit greater stability as calcination temperature increases. The more ordered crystalline surface at higher calcination temperature has greater charge distribution and hence stronger zeta potential values. Also, higher calcination temperatures cause redistribution of Co^{2+} and Fe^{3+} ions between tetrahedral and octahedral locations in the spinel structure, which results in different surface charge density and electrical double layer properties.[51] Thus, they can be used for many applications including magnetic drug delivery systems and magnetic hyperthermia for cancer therapy as they can stay stable in solutions and avoid formation of clumps that can decrease the heating efficiency. They can also be used in magnetic resonance imaging (MRI), catalysts, data storage devices, sensors and magneto-optical devices.

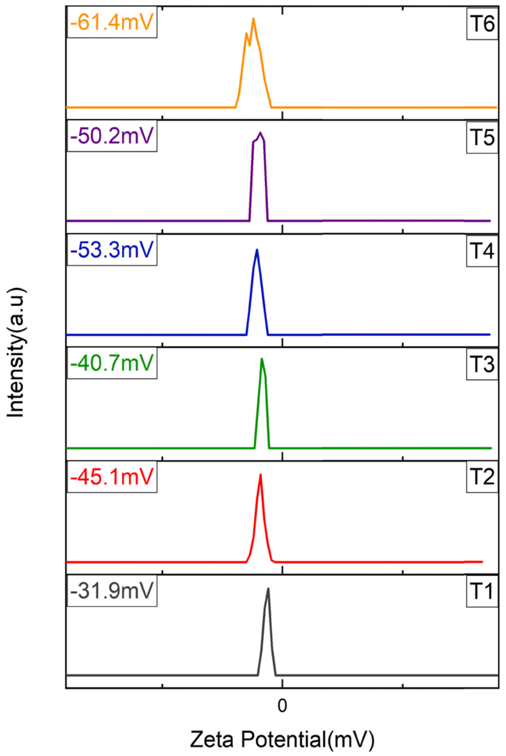

Fig. 13 Zeta potential results of T1, T2, T3, T4, T5 and T6 samples.

Table 5 Zeta potential values of the $CoFe_2O_4$ samples (T1, T2, T3, T4, T5 and T6)

Sample	Calcination temp. (°C)	Crystal size (nm)	Zeta potential (mV)
T1	500	4.17	−31.90
T2	600	7.82	−45.10
T3	700	9.52	−40.28
T4	800	15.92	−53.30
T5	900	19.33	−50.20
T6	1000	19.59	−62.40

4 Conclusion

This study concludes that the sol–gel method can be used to synthesize different crystallite sizes at different calcination temperatures. The lattice strain and crystallite size determination using SSP and H–W methods proved the production of crystalline nanoparticles. XRD values justify that with increase in the temperature of calcination the size of the crystalline nanoparticles increases. The VSM results showed that the magnetic coercivity decreased while the saturation magnetization increased as the calcination temperature increased for samples T1–T6. FTIR confirms cobalt ferrite nanoparticle formation due to the M–O bond vibrational peaks. The dielectric constant decreased with rising temperature and as the crystal size increases it is found that the band energy gap decreases. The zeta potential also proved that the nanoparticles are more stable at higher temperatures. Thus, there is no denying that with different calcination temperatures (500 °C, 600 °C, 700 °C, 800 °C, 900 °C, and 1000 °C) the size of the crystalline cobalt ferrite nanoparticles varies greatly. These results can be used to synthesize and modify nanoparticles with better characteristics using the sol–gel method.

Author contributions

Md. Farid Ahmed: conceptualization, methodology, resources, project administration, supervision, funding acquisition visualization, writing – review and editing; Afia Yasmin: writing – original draft preparation, investigation, formal analysis, software, data curation, writing – review and editing; Bristy Biswas: validation, resourcnes, writing – review and editing; MD. Lutfor Rahman: validation, resources, writing – review and editing; Juliya Khanam: validation, resources, writing – review and editing; Rabeya Jahan Rakhi: validation, resources, writing – review and editing; Dipa Islam: validation, resources, writing – review and editing, Md. Sahadat Hossain: validation, resources, writing – review and editing; Firoz Ahmed: formal analysis; Israt Jahan Lithi: writing – review and editing; Nahid Sharmin: project administration, supervision, writing – review and editing.

Conflicts of interest

The authors declare that they have no known conflict of interest.

Data availability

Data will be made available upon request.

Acknowledgements

This work was supported by the Ceramic Raw Materials & Ceramic Materials Testing Division, Institute of Glass and Ceramic Research & Testing (IGCRT), IGCRT and Fibre & Polymer Research Division, Dhaka Labs BCSIR, Bangladesh Council of Scientific and Industrial Research (BCSIR), Dhaka, Bangladesh. The authors also acknowledge the financial support from the BCSIR authority through the approved R&D project (no. 39.02.0000.011.14.169.2023/877, date: 17.09.2023).

References

1 I. Jahan Lithi, K. I. A. Nakib, A. M. Sarwaruddin Chowdhury and M. S. Hossain, A review on the green synthesis of metal (Ag, Cu, and Au) and metal oxide (ZnO, MgO, Co_3O_4, and TiO_2) nanoparticles using plant extracts for developing antimicrobial properties, *Nanoscale Adv.*, 2025, **7**, 2446–2473, DOI: **10.1039/D5NA00037H**.

2 W. Chen, C.-A. Cheng and J. I. Zink, Spatial, Temporal, and Dose Control of Drug Delivery using Noninvasive Magnetic Stimulation, *ACS Nano*, 2019, **13**(2), 1292–1308, DOI: **10.1021/acsnano.8b06655**.

3 A. Avasthi, C. Caro, E. Pozo-Torres, M. P. Leal and M. L. García-Martín, Magnetic nanoparticles as MRI contrast agents, *Surf.-Modif. Nanobiomater. Electrochem. Biomed. Appl.*, 2020, 49–91.

4 P. N. Anantharamaiah, H. M. Shashanka, R. Kumar, J. A. Chelvane and B. Sahoo, Chemically enabling $CoFe_2O_4$ for magnetostrictive strain sensing applications at lower magnetic fields: effect of Zn substitution, *Mater. Sci. Eng., B*, 2021, **266**, 115080.

5 M. Mousavi-Kamazani, S. Zinatloo-Ajabshir and M. Ghodrati, One-step sonochemical synthesis of $Zn(OH)_2/ZnV_3O_8$ nanostructures as a potent material in electrochemical hydrogen storage, *J. Mater. Sci.: Mater. Electron.*, 2020, **31**(20), 17332–17338.

6 S. Zinatloo-Ajabshir, M. Baladi and M. Salavati-Niasari, Enhanced visible-light-driven photocatalytic performance for degradation of organic contaminants using $PbWO_4$ nanostructure fabricated by a new, simple and green sonochemical approach, *Ultrason. Sonochem.*, 2021, **72**, 105420.

7 S. Zinatloo-Ajabshir and M. Mousavi-Kamazani, Effect of copper on improving the electrochemical storage of hydrogen in CeO_2 nanostructure fabricated by a simple and surfactant-free sonochemical pathway, *Ceram. Int.*, 2020, **46**(17), 26548–26556.

8 B. F. Bogacz, R. Gargula, P. Kurzydło, A. T. Pędziwiatr, T. Tatarchuk and N. Paliychuk, Two-Level Model Description of Superparamagnetic Relaxation in Nanoferrites $(Co,Zn)Fe_2\ O_4$, *Acta Phys. Pol., A*, 2018, **134**(5), 993–998, DOI: 10.12693/APhysPolA.134.993.

9 M. S. Al Maashani, K. A. Khalaf, A. M. Gismelseed and I. A. Al-Omari, The structural and magnetic properties of the nano-$CoFe_2O_4$ ferrite prepared by sol-gel auto-combustion technique, *J. Alloys Compd.*, 2020, **817**, 152786, DOI: 10.1016/j.jallcom.2019.152786.

10 A. Omelyanchik, G. Singh, M. Volochaev, A. Sokolov, V. Rodionova and D. Peddis, Tunable magnetic properties of Ni-doped $CoFe_2O_4$ nanoparticles prepared by the sol–gel citrate self-combustion method, *J. Magn. Magn. Mater.*, 2019, **476**, 387–391, DOI: 10.1016/j.jmmm.2018.12.064.

11 V. P. Senthil, J. Gajendiran, S. G. Raj, T. Shanmugavel, G. Ramesh Kumar and C. Parthasaradhi Reddy, Study of structural and magnetic properties of cobalt ferrite ($CoFe_2O_4$) nanostructures, *Chem. Phys. Lett.*, 2018, **695**, 19–23, DOI: 10.1016/j.cplett.2018.01.057.

12 P. Thakur, N. Gahlawat, P. Punia, S. Kharbanda, B. Ravelo and A. Thakur, Cobalt Nanoferrites: a Review on Synthesis, Characterization, and Applications, *J. Supercond. Nov. Magn.*, 2022, **35**(10), 2639–2669, DOI: 10.1007/s10948-022-06334-1.

13 A. H. Ashour, *et al.*, Antimicrobial activity of metal-substituted cobalt ferrite nanoparticles synthesized by sol–gel technique, *Particuology*, 2018, **40**, 141–151, DOI: 10.1016/j.partic.2017.12.001.

14 R. Jasrotia, *et al.*, Cobalt ferrites: structural insights with potential applications in magnetics, dielectrics, and Catalysis, *Coord. Chem. Rev.*, 2025, **522**, 216198, DOI: 10.1016/j.ccr.2024.216198.

15 R. Jabbar, S. H. Shahatha, N. K. Taieh, B. Magid and A. F. Showard, Preparation and study of the effect of pH value on structural, morphological, electrical and magnetic properties of $CoFe_2O_4$ nanoparticles prepared by sol-gel precipitation method, *Ceram. Int.*, 2024, **50**(17, Part B), 31114–31123, DOI: 10.1016/j.ceramint.2024.05.417.

16 M. N. Kiani, *et al.*, Synthesis and Characterization of Cobalt-Doped Ferrites for Biomedical Applications, *ACS Omega*, 2023, **8**(4), 3755–3761, DOI: 10.1021/acsomega.2c05226.

17 D. A. Gole, S. B. Kapatkar, S. N. Mathad and R. R. Chavan, In vitro antimicrobial activity of cobalt ferrite nanoparticles synthesized by Co-precipitation method, *Acta Chem. Iasi*, 2020, **28**(2), 225–236.

18 T. Zhang, *et al.*, Stoichiometric-Induced Cationic Inversion of Cobalt Ferrite for High-Sensitivity Acetone Gas Sensor and Mechanistic Insight, *ACS Appl. Electron. Mater.*, 2025, **7**(1), 369–379, DOI: 10.1021/acsaelm.4c01803.

19 N. C. S. de Souza, G. Alves Puiatti, G. do, C. Dias, R. Matias Silva, R. P. Lopes Lopes and T. Almeida Silva, Development of sustainable electrodes based on cobalt ferrite decorated biochar for the voltammetric determination of paracetamol at biological fluid, *Anal. Methods*, 2025, **17**, 3509–3516, DOI: 10.1039/D5AY00089K.

20 C. E. D. Cardoso, J. C. Almeida, J. Rocha and E. Pereira, Uptake of Phosphorus from an Acidic Kraft Pulp Industrial Effluent Using Magnetic Nanoparticles, *ACS Sustainable Resour. Manage.*, 2025, **2**(2), 267–274, DOI: 10.1021/acssusresmgt.4c00346.

21 M. Bekhit, A. S. Orabi, F. Mohamad and K. M. A. El-Nour, A facile one-pot γ-radiation formation of gum arabic-stabilized cobalt ferrite nanoparticles as an efficient magnetically retrievable heterogeneous catalyst, *RSC Adv.*, 2025, **15**(12), 9119–9128, DOI: 10.1039/D5RA00651A.

22 R. Prosper Medang, *et al.*, Green synthesis of cobalt ferrite from rotten passion fruit juice and application as an electrocatalyst for the hydrogen evolution reaction, *Energy Adv.*, 2024, **3**(6), 1367–1374, DOI: 10.1039/D3YA00450C.

23 A. Saremi, S. M. Mirkazemi, A. Sazvar and H. Rezaie, Controlling magnetic and surface properties of cobalt ferrite nanoparticles: a comparison of co-precipitation and solvothermal synthesis methods, *Solid State Sci.*, 2024, **148**, 107432.

24 V. R. Bhagwat, A. V. Humbe, S. D. More and K. M. Jadhav, Sol-gel auto combustion synthesis and characterizations of cobalt ferrite nanoparticles: different fuels approach, *Mater. Sci. Eng., B*, 2019, **248**, 114388, DOI: 10.1016/j.mseb.2019.114388.

25 Y. Iqbal, *et al.*, Optimizing the magnetic field strength and concentration of silica coated cobalt ferrite nanoparticles for magnetic hyperthermia, *Inorg. Chem. Commun.*, 2024, **167**, 112796, DOI: 10.1016/j.inoche.2024.112796.

26 K. Prabakaran, *et al.*, Pyrolytic carbon decorated cobalt ferrite nanostructures as a negative electrode material for improved supercapacitor applications, *Diamond Relat. Mater.*, 2025, **151**, 111822, DOI: 10.1016/j.diamond.2024.111822.

27 A. L. Gurgel, A. E. Martinelli, O. L. de Aquino Conceição, M. M. Xavier Jr, M. A. M. Torres and D. M. de Araújo Melo,

Microwave-assisted hydrothermal synthesis and magnetic properties of nanostructured cobalt ferrite, *J. Alloys Compd.*, 2019, **799**, 36–42.

28 S. B. Mohammed, T. H. Mubarak and Y. Alnaiemy, Impact of Mn^{2+} Doping on the Structure, Morphology, and Magnetic Properties of Cobalt Ferrite Nanoparticles Synthesized Using Sol–Gel Auto-combustion Technique, *Semiconductors*, 2025, **59**(2), 167–182, DOI: **10.1134/S1063782624602188**.

29 S. Ahmad, *et al.*, Magnetic properties of different phases iron oxide nanoparticles prepared by micro emulsion-hydrothermal method, *Sci. Rep.*, 2025, **15**(1), 878, DOI: **10.1038/s41598-025-85145-5**.

30 T. Tatarchuk, A. Shyichuk, V. Kotsyubynsky and N. Danyliuk, Catalytically active cobalt ferrites synthesized using plant extracts: insights into structural, optical, and catalytic properties, *Ceram. Int.*, 2025, **51**(4), 4988–4999, DOI: **10.1016/j.ceramint.2024.11.470**.

31 V. K. Raut, S. B. Somvanshi, E. A. Dawi and C. T. Birajdar, Sol-gel auto combustion synthesis of Al^{3+}–Gd^{3+} ions co-doped cobalt ferrite nanoparticles for nanoelectronics applications, *J. Sol-Gel Sci. Technol.*, 2024, **112**(3), 738–751.

32 T. A. Mohaymen Taha, A. S. Abouhaswa and W. S. Mohamed, Enhanced catalytic performance of magnetic zinc-doped cobalt ferrite nanoparticles in sodium borohydride methanolysis, *Int. J. Hydrogen Energy*, 2025, **112**, 133–143, DOI: **10.1016/j.ijhydene.2025.02.373**.

33 T. Ramesh, V. Madhavi, P. V. Rao, K. Vagdevi, N. Basavegowda and K.-H. Baek, Impact of ultrasonic-assisted co-precipitation synthesis and ultrasonication duration on cobalt ferrite nanostructures: a comparative study of structural, morphological, optical and magnetic properties, *Inorg. Chem. Commun.*, 2025, 114035.

34 A. S. Joseph, *et al.*, Solvothermal synthesis of ruthenium-doped cobalt ferrite nanoparticles – A feasible approach to modify the magnetic properties and nonlinear optical absorption, *Mater. Sci. Semicond. Process.*, 2025, **188**, 109246, DOI: **10.1016/j.mssp.2024.109246**.

35 O. S. Ivanova, *et al.*, Impact of annealing temperature on the structure, magnetic properties, and organic dyes adsorption capacity of $Fe_{0.5}Co_{2.5}O_4$ nanoparticles obtained by combustion, *J. Alloys Compd.*, 2025, **1011**, 178421, DOI: **10.1016/j.jallcom.2024.178421**.

36 E. Swatsitang, *et al.*, Characterization and magnetic properties of cobalt ferrite nanoparticles, *J. Alloys Compd.*, 2016, **664**, 792–797, DOI: **10.1016/j.jallcom.2015.12.230**.

37 S. M. Hashemi, Z. Ataollahi, S. Hasani and A. Seifoddini, Synthesis of the cobalt ferrite magnetic nanoparticles by sol–gel auto-combustion method in the presence of egg white (albumin), *J. Sol-Gel Sci. Technol.*, 2023, **106**(1), 23–36, DOI: **10.1007/s10971-023-06073-2**.

38 M. Podder, Md. F. Ahmed, Md. R. Moni, Md. L. Rahman, B. Biswas and N. Sharmin, Effect of metal ions on structural, morphological and optical properties of nano-crystallite spinel cobalt-aluminate ($CoAl_2O_4$), *Arab. J. Chem.*, 2023, **16**(5), 104700, DOI: **10.1016/j.arabjc.2023.104700**.

39 R. P. Sharma, S. D. Raut, R. M. Mulani, A. S. Kadam and R. S. Mane, Sol–gel auto-combustion mediated cobalt ferrite nanoparticles: a potential material for antimicrobial applications, *Int. Nano Lett.*, 2019, **9**(2), 141–147, DOI: **10.1007/s40089-019-0268-4**.

40 M. F. Ahmed, *et al.*, Investigation the effect of calcination heating rate on the structural, morphological, thermal and color properties of nano Cobalt Aluminate ($CoAl_2O_4$), *Heliyon*, 2025, **11**(3), e42413, DOI: **10.1016/j.heliyon.2025.e42413**.

41 Md Sahadat Hossain and S. Ahmed, Easy and green synthesis of TiO_2 (Anatase and Rutile): estimation of crystallite size using Scherrer equation, Williamson-Hall plot, Monshi-Scherrer Model, size-strain plot, Halder–Wagner Model, *Results Mater.*, 2023, **20**, 100492, DOI: **10.1016/j.rinma.2023.100492**.

42 J. S. Lim and F. K. Yam, Structural parameters of CVD synthesized Ga_2O_3 nanostructures from X-ray diffraction analysis derived by Scherrer, Williamson-Hall, Size-Strain Plot and Halder–Wagner methods–A comparative study, *Phys. B*, 2025, **699**, 416798, DOI: **10.1016/j.physb.2024.416798**.

43 K. Patel, A. Patel, V. P. Jethwa, H. Patel and G. K. Solanki, X-ray diffraction analysis of orthorhombic SnSe nanoparticles by Williamson–Hall, Halder–Wagner and Size–Strain plot methods, *Chem. Phys. Impact*, 2024, **8**, 100547, DOI: **10.1016/j.chphi.2024.100547**.

44 Md. K. Alam, Md. S. Hossain, N. M. Bahadur and S. Ahmed, A comparative study in estimating of crystallite sizes of synthesized and natural hydroxyapatites using Scherrer Method, Williamson-Hall model, Size-Strain Plot and Halder–Wagner Method, *J. Mol. Struct.*, 2024, **1306**, 137820, DOI: **10.1016/j.molstruc.2024.137820**.

45 M. Rabiei, A. Palevicius, A. Monshi, S. Nasiri, A. Vilkauskas and G. Janusas, Comparing Methods for Calculating Nano Crystal Size of Natural Hydroxyapatite Using X-Ray Diffraction, *Nanomaterials*, 2020, **10**(9), 1627, DOI: **10.3390/nano10091627**.

46 Md Sahadat Hossain and S. Ahmed, Sustainable synthesis of nano CuO from electronic waste (E-waste) cable: evaluation of crystallite size via Scherrer equation, Williamson–Hall plot, Halder–Wagner model, Monshi–Scherrer model, size-strain plot, *Results Eng.*, 2023, **20**, 101630, DOI: **10.1016/j.rineng.2023.101630**.

47 V. Mote, Y. Purushotham and B. Dole, Williamson-Hall analysis in estimation of lattice strain in nanometer-sized ZnO particles, *J. Theor. Appl. Phys.*, 2012, **6**(1), 6, DOI: **10.1186/2251-7235-6-6**.

48 H. Jalili, B. Aslibeiki, A. Ghotbi Varzaneh and V. A. Chernenko, The effect of magneto-crystalline anisotropy on the properties of hard and soft magnetic ferrite nanoparticles, *Beilstein J. Nanotechnol.*, 2019, **10**, 1348–1359, DOI: **10.3762/bjnano.10.133**.

49 A. Zeleňáková, *et al.*, Cobalt-ferrite nano-cubes for magnetic hyperthermia applications, *J. Alloys Compd.*, 2024, **989**, 174415, DOI: **10.1016/j.jallcom.2024.174415**.

50 H. Jalili, B. Aslibeiki, A. Hajalilou, O. Musalu, L. P. Ferreira and M. M. Cruz, Bimagnetic hard/soft and soft/hard ferrite nanocomposites: structural, magnetic and hyperthermia

properties, *Ceram. Int.*, 2022, **48**(4), 4886–4896, DOI: 10.1016/j.ceramint.2021.11.025.

51 T. Prabhakaran, R. V. Mangalaraja, J. C. Denardin and J. A. Jiménez, The effect of calcination temperature on the structural and magnetic properties of co-precipitated $CoFe_2O_4$ nanoparticles, *J. Alloys Compd.*, 2017, **716**, 171–183.

52 M. Basak, M. L. Rahman, M. F. Ahmed, B. Biswas and N. Sharmin, Calcination effect on structural, morphological and magnetic properties of nano-sized $CoFe_2O_4$ developed by a simple co-precipitation technique, *Mater. Chem. Phys.*, 2021, **264**, 124442.

53 Z. Mosleh, M. Beygmohammadvand, A. G. Varzaneh and P. Kameli, Influence of cobalt substitution in $CoFe_2O_4$ nanoparticles on structural, morphological, cation distribution, optical and magnetic properties, *Heliyon*, 2025, **11**(1), e41276.

54 P. H. Nam, *et al.*, Physical characterization and heating efficacy of chitosan-coated cobalt ferrite nanoparticles for hyperthermia application, *Phys. E*, 2021, **134**, 114862, DOI: 10.1016/j.physe.2021.114862.

55 A. Das, K. K. Bestha, P. Bongurala and V. Gorige, Correlation between size, shape and magnetic anisotropy of $CoFe_2O_4$ ferrite nanoparticles, *Nanotechnology*, 2020, **31**(33), 335716.

56 Z. Mahhouti, *et al.*, Chemical synthesis and magnetic properties of monodisperse cobalt ferrite nanoparticles, *J. Mater. Sci.: Mater. Electron.*, 2019, **30**(16), 14913–14922, DOI: 10.1007/s10854-019-01863-3.

57 A. Mazzoli and O. Favoni, Particle size, size distribution and morphological evaluation of airborne dust particles of diverse woods by Scanning Electron Microscopy and image processing program, *Powder Technol.*, 2012, **225**, 65–71, DOI: 10.1016/j.powtec.2012.03.033.

58 A. Venkatesan, *et al.*, Synthesis, characterization and magnetic properties of Mg^{2+} doped green pigment Cobalt aluminate nanoparticles, *J. Mater. Sci.: Mater. Electron.*, 2022, **33**(27), 21246–21257, DOI: 10.1007/s10854-022-08834-1.

59 C. Wang, X. Bai, S. Liu and L. Liu, Synthesis of cobalt-aluminum spinels via EDTA chelating precursors, *J. Mater. Sci.*, 2004, **39**(20), 6191–6201, DOI: 10.1023/B:JMSC.0000043586.66653.de.

60 X. Wei and D. Chen, Synthesis and characterization of nanosized zinc aluminate spinel by sol–gel technique, *Mater. Lett.*, 2006, **60**(6), 823–827, DOI: 10.1016/j.matlet.2005.10.024.

61 S. M. A. R. Hussam and A. Khader, XRD and SEM characteristics of Co–Ni ferrite nanoparticles Synthesized using sol-gel method, *Turk. J. Comput. Math. Educ.*, 2021, **12**(14), 675–687.

62 A. Hossain, M. S. I. Sarker, M. K. R. Khan, F. A. Khan, M. Kamruzzaman and M. M. Rahman, Structural, magnetic, and electrical properties of sol–gel derived cobalt ferrite nanoparticles, *Appl. Phys. A: Mater. Sci. Process.*, 2018, **124**(9), 608, DOI: 10.1007/s00339-018-2042-2.

63 L. Zhao, *et al.*, Studies on the magnetism of cobalt ferrite nanocrystals synthesized by hydrothermal method, *J. Solid State Chem.*, 2008, **181**(2), 245–252, DOI: 10.1016/j.jssc.2007.10.034.

64 P. Jain, S. Shankar and O. P. Thakur, Advancements in multiferroic, dielectric, and impedance properties of copper–yttrium co-doped cobalt ferrite for hydroelectric cell applications, *J. Phys.: Condens. Matter*, 2024, **36**(29), 295201.

65 A. M. Mohammad, S. A. Ridha and T. H. Mubarak, Dielectric properties of Cr-substituted cobalt ferrite nanoparticles synthesis by citrate-gel auto combustion method, *Int. J. Appl. Eng. Res.*, 2018, **13**(8), 6026–6035.

66 P. G. Ravi Kumar Vijai, Synthesis, Characterization and Dielectric properties of Nanoparticles of Cobalt Doped Ferrite ($Co_xFe_{1-x}Fe_2O_4$), *Int. J. Chem. Math. Phys. IJCMP*, 2023, **7**(4), 1–8.

67 T. Javed, A. Maqsood and A. A. Malik, Structural, Electrical and Dielectric Properties of Co–Mn Spinel Nanoferrites Prepared by Co-precipitation Technique, *J. Supercond. Nov. Magn.*, 2011, **24**(7), 2137–2144, DOI: 10.1007/s10948-011-1168-7.

68 S. Jabez, S. Mahalakshmi and S. Nithiyanantham, Frequency and temperature effects on dielectric properties of cobalt ferrite, *J. Mater. Sci.: Mater. Electron.*, 2017, **28**(7), 5504–5511, DOI: 10.1007/s10854-016-6212-8.

69 A. M. El Nahrawy, A. M. Mansour, A. B. Abou Hammad and A. R. Wassel, Effect of Cu incorporation on morphology and optical band gap properties of nano-porous lithium magneso-silicate (LMS) thin films, *Mater. Res. Express*, 2018, **6**(1), 016404, DOI: 10.1088/2053-1591/aae343.

70 N. Dhanda, P. Thakur and A. Thakur, Green synthesis of cobalt ferrite: a study of structural and optical properties, *Mater. Today Proc.*, 2023, **73**, 237–240, DOI: 10.1016/j.matpr.2022.07.202.

71 K. Kahouli, A. B. J. Kharrat and S. Chaabouni, Optical properties analysis of the new $(C_9H_{14}N)_3BiCl_6$ compound by UV-visible measurements, *Indian J. Phys.*, 2021, **95**(12), 2797–2805, DOI: 10.1007/s12648-020-01942-w.

72 S. Swathi, R. Yuvakkumar, P. S. Kumar, G. Ravi and D. Velauthapillai, Annealing temperature effect on cobalt ferrite nanoparticles for photocatalytic degradation, *Chemosphere*, 2021, **281**, 130903, DOI: 10.1016/j.chemosphere.2021.130903.

73 N. M. Refat, M. Y. Nassar and S. A. Sadeek, A controllable one-pot hydrothermal synthesis of spherical cobalt ferrite nanoparticles: synthesis, characterization, and optical properties, *RSC Adv.*, 2022, **12**(38), 25081–25095, DOI: 10.1039/D2RA03345C.

74 V. Madhavi, T. N. V. K. V. Prasad, A. V. B. Reddy, B. Ravindra Reddy and G. Madhavi, Application of phytogenic zerovalent iron nanoparticles in the adsorption of hexavalent chromium, *Spectrochim. Acta, Part A*, 2013, **116**, 17–25, DOI: 10.1016/j.saa.2013.06.045.

75 A. Manohar and C. Krishnamoorthi, Magnetic and photocatalytic studies on $Zn_{1-x}Mg_xFe_2O_4$ nanocolloids synthesized by solvothermal reflux method, *J. Photochem. Photobiol., B*, 2017, **177**, 95–104, DOI: 10.1016/j.jphotobiol.2017.10.009.